Solar RRL
www.solar-rrl.com

Low-Cost Dopant-Free Carbazole Enamine Hole-Transporting Materials for Thermally Stable Perovskite Solar Cells

Suer Zhou, Maryte Daskeviciene, Matas Steponaitis, Giedre Bubniene, Vygintas Jankauskas, Kelly Schutt, Philippe Holzhey, Ashley R. Marshall, Pietro Caprioglio, Grey Christoforo, James M. Ball, Tadas Malinauskas, Vytautas Getautis, and Henry J. Snaith**

Perovskite solar cells deliver high efficiencies, but are often made from high-cost bespoke chemicals, such as the archetypical hole-conductor, 2,2′,7,7′-tetrakis(*N*,*N*-di-*p*-methoxy-phenylamine)-9-9′-spirobifluorene (spiro-OMeTAD). Herein, new charge-transporting carbazole-based enamine molecules are reported. The new hole conductors do not require chemical oxidation to reach high power conversion efficiencies (PCEs) when employed in *n*-type-intrinsic-*p*-type perovskite solar cells; thus, reducing the risk of moisture degrading the perovskite layer through the hydrophilicity of oxidizing additives that are typically used with conventional hole conductors. Devices made with these new undoped carbazole-based enamines achieve comparable PCEs to those employing doped spiro-OMeTAD, and greatly enhanced stability under 85 °C thermal aging; maintaining 83% of their peak efficiency after 1000 h, compared with spiro-OMeTAD-based devices that degrade to 26% of the peak PCE within 24 h. Furthermore, the carbazole-based enamines can be synthesized without the use of organometallic catalysts and complicated purification techniques, lowering the material cost by one order of magnitude compared with spiro-OMeTAD. As a result, we calculate that the overall manufacturing costs of future photovoltaic (PV) modules are reduced, making the levelized cost of electricity competitive with silicon PV modules.

1. Introduction

The very first report of perovskite solar cells (PSCs) was published in 2009 and described a device producing 3.8% power conversion efficiency (PCE) employing a liquid electrolyte redox couple.[1] Spurring a dearth of activity in the following 3 years, reports of over 10% efficient perovskite solar cells employing solid-state hole conductors in 2012,[2,3] the perovskite solar cell research field exploded into life. As a result, a phenomenal amount of research has been done since then and the performance of PSCs raised dramatically, reaching a certified PCE of 25.5% in 2021 for a single junction device.[4] The device architecture, the composition of perovskite, processing methodologies, and electron extraction layers, have all changed considerably since the first early reports. However, the hole conductor, 2,2′,7,7′-tetrakis(*N*,*N*-di-*p*-methoxy-phenylamine)-9-9′-spirobifluorene (spiro-OMeTAD), along with a "cocktail" of ionic and basic additives, remains essentially unaltered in the highest efficiency perovskite cells.[5–7] This extraction layer was first employed in the first solid-state perovskite cells reported in 2012, and originated in solid-state dye-sensitized solar cells from 1998.[8]

S. Zhou, K. Schutt, P. Holzhey, A. R. Marshall, P. Caprioglio, G. Christoforo, J. M. Ball, H. J. Snaith
Department of Physics, Clarendon Laboratory
University of Oxford Parks Road
Oxford OX1 3PU, UK
E-mail: henry.snaith@physics.ox.ac.uk

The ORCID identification number(s) for the author(s) of this article can be found under https://doi.org/10.1002/solr.202100984.

DOI: 10.1002/solr.202100984

M. Daskeviciene, M. Steponaitis, G. Bubniene, T. Malinauskas, V. Getautis
Department of Organic Chemistry
Kaunas University of Technology
Kaunas LT-50254, Lithuania
E-mail: vytautas.getautis@ktu.lt

V. Jankauskas
Institute of Chemical Physics
Vilnius University
Vilnius LT-10222, Lithuania

Despite the promises of this technology, PSCs can degrade due to a variety of reasons[9–11] and moisture is one of the key culprits.[12] The best performing perovskite materials are usually comprised of a mixture of multiple small organic and inorganic monocations, lead(II) cations, and halide anions.[13] When such perovskites interact with water, they can form an intermediate hydrated structure, followed by degradation to lead halide, which leads to a large drop in PCE.[14–16] One of the possible pathways for moisture to reach the perovskite layer is through the hygroscopic dopants (ionic and basic additives) used to induce chemical oxidation that improves conductivity and photoelectric properties of the hole-transporting materials (HTMs).[17] For example, one commonly used dopant, bis(trifluoromethane)sulfonimide lithium salt (Li-TFSI), is hygroscopic.[18] Doping increases the conductivity of commonly-used HTMs by increasing the hole density, since conductivity is proportional to the product of the hole density and mobility.[19–21] However, it is preferable to improve the inherent mobility of the HTMs because doping can lead to additional instabilities.

Different doping strategies can be applied to boost the performance of the HTM, such as oxidation in air, the addition of chemical oxidization agents (such as cobalt-based metal complexes),[22] direct addition of presynthesized HTM^+ bis(trifluoromethane)sulfonimide $(TFSI)^-$ and the use of chemical adducts.[23–25] For instance, the most widely used hole-transporting material for devices in the *n-i-p* configuration is spiro-OMeTAD, which has low conductivity in its pure form. It is commonly doped with Li-TFSI, 4-tert-butyl pyridine (*t*BP), and cobalt-based metal complexes (for example tris(2-(1H-pyrazol-1-yl)-4-tert-butylpyridine)cobalt(III) tri[bis(trifluoromethane)sulfonimide]) (FK209).[22] If Li-TFSI is used without the cobalt salt, the oxidation process depends on prolonged ambient oxygen exposure and therefore suffers from poor control over doping levels.[26] The FK209 partially oxidizes spiro-OMeTAD by reducing Co(III) to Co(II), thus initially increasing the HTM conductivity. To further oxidize spiro-OMeTAD, air oxidation with Li-TFSI is still needed to deliver the most efficient solar cells.[18,27,28] The addition of lithium ions can contaminate other parts of the device, potentially lowering the PCE over time, such as lithium-ion migration causing increased hysteresis.[29,30]

The presence of *t*BP was also shown to reduce the glass-transition temperature of spiro-OMeTAD below 100 °C.[31] Adding *t*BP along with Li-TFSI further causes morphological transformations at the perovskite/spiro-OMeTAD interface at elevated temperatures (>85 °C), which decreases device efficiencies.[32,33] Therefore, it is desirable to avoid chemical oxidation and additives for better device stability, thus making "dopant-free" HTMs very attractive alternatives. There are two main types of dopant-free HTMs for the common (*n-i-p*) device architecture: polymers and small molecules. Polymers tend to demonstrate better device PCEs, possibly due to the ability to coat thinner uniform films, in comparison with their small molecule counterparts. However, they suffer from drawbacks, such as purity, batch-to-batch reproducibility,[34] and higher synthetic costs.[35] In contrast, the PCEs of small-molecule, additive-free HTMs are typically around 15%, with very few examples over 18%.[36–38] Nevertheless, the synthesis of these small molecules, p-type semiconductors is reproducible; they can be purified in many different ways and, similarly to dopant-free polymers, increase the long-term stability of devices.[35]

In this study, we describe the synthesis and application of new carbazole-based enamines as HTMs, specifically, N^3, N^3, N^6, N^6, 9-pentakis[2,2-bis(-methoxyphenyl)ethenyl]-9 *H*-carbazole-3,6-diamine (MeO5PECz) and N^3, N^3, N^6, N^6, 9-tetrakis[2,2-bis(-methoxyphenyl)ethenyl]-9-butyl-9 *H*-carbazole-3,6-diamine (MeO4PEBCz) (**Figure 1**a). These materials are the product of a facile synthesis that avoids expensive organometallic catalysts or costly purification techniques, resulting in significantly reduced cost from 92$ g^{-1} for spiro-OMeTAD[39] to 7.83 $ g^{-1} for MeO5PECz and 10.33$ g^{-1} for MeO4PEBCz. Furthermore, no chemical oxidation or dopants are required to reach high PCEs, making these materials attractive alternatives for applications in PSCs.

2. Results and discussion

The synthesis of enamines MeO5PECz and MeO4PEBCz from commercially available carbazole diamines are shown in Figure 1a,b.

Carbazole derivatives MeO5PECz and MeO4PEBCz have been obtained without the use of expensive palladium-catalyzed cross-coupling in a simple, acid-catalyzed condensation reaction between carbazole diamines and bis(4-methoxyphenyl)-acetaldehyde (Figure 1a,b). The MeO5PECz and MeO4PEBCz were purified by recrystallization, without the need for column chromatography.

The UV-vis absorption was performed on thin films of the HTMs on glass substrates (Figure 1c). The π–π^* transition of MeO4PEBCz can be seen at 353 nm and of MeO5PECz at 358 nm.

Photoemission spectroscopy in air was used to measure the ionization potential (I_p) of the carbazole derivatives in the solid-state (the error is estimated to be ±0.03 eV) (Figure S8 and S9). All materials have similar I_p of near 5.00 eV (**Table 1**); interestingly, the additional electron donating bis(4-methoxyphenyl)ethenyl moiety in MeO5PECz increases the I_p slightly compared with MeO4PEBCz. Steric hindrance, resulting from five bis(4-methoxyphenyl)ethenyl fragments connected to the carbazole core, could be the main factor behind the small differences in I_p, since it influences the electronic coupling between the peripheral phenyl units and the carbazole core. In this case, the one additional bis(4-methoxyphenyl)ethenyl group in MeO5PECz increases the steric hindrance around the carbazole core, thus forcing other phenylethenyl fragments to adopt a less planar configuration, mitigating the electron donor impact of the substituents.

The thermal stability of the HTMs was determined using thermogravimetric analysis (TGA), the results are shown in Figure S1 and Table S1, Supporting Information. The materials demonstrated 5% weight loss just slightly below 400 °C, showing that they are sufficiently thermally stable for application in PSCs. Furthermore, the rapid weight loss seen in Figure S1, Supporting Information, just below 450 °C suggests that the investigated materials can readily sublime and demonstrate the potential for vacuum deposition.

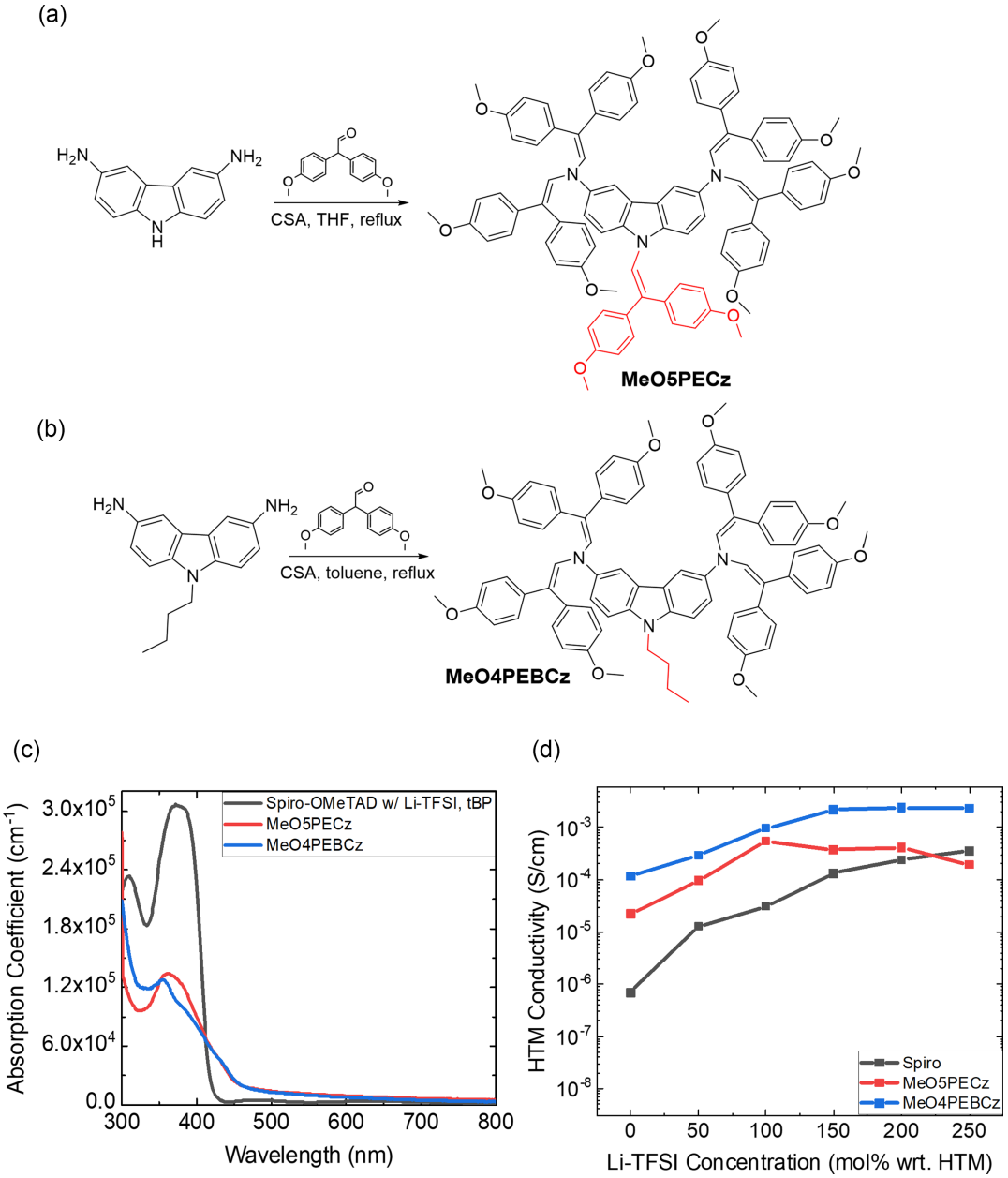

Figure 1. a) Synthesis of carbazole enamines MeO5PECz and b) MeO4PEBCz. c) UV-vis absorption spectra of carbazole derivatives MeO5PECz, MeO4PEBCz, and spiro-OMeTAD thin films on glass. d) Conductivity of spiro-OMeTAD, MeO5PECz, and MeO4PEBCz variation with Li-TFSI doping concentration (after having been left in a dessicator box with silica gel for 24 h), measured with a 4-point probe.

Table 1. Photophysical properties of the synthesized materials and spiro-OMeTAD for comparison.

Compound	I_p, [eV][a)]	μ_0 [$cm^2 V^{-1} s^{-1}$][b)]	μ [$cm^2 V^{-1} s^{-1}$] [c)]	α[d)]
MeO5PECz	5.01	3.7×10^{-5}	7.8×10^{-4}	0.0038
MeO4PEBCz	4.96	1.2×10^{-4}	1.1×10^{-3}	0.0027
Spiro-OMeTAD[23]	5.00	4.1×10^{-5}	5×10^{-4}	0.0031

[a)]Ionization potential was measured on films by photoemission spectroscopy in air; [b)]hole mobility value at zero field strength; [c)]hole mobility value at the electric field strength of 6.4×10^5 V cm^{-1} [d)]Poole–Frenkel parameter.

Under working conditions, PSCs can reach temperatures well above 65 °C[40]; therefore, HTMs must have glass transition temperatures (T_g) above 65 °C. The T_g of the enamines was measured using differential scanning calorimetry (DSC) and the results show that both MeO5PECz and MeO4PEBCz have acceptable T_g, 152 and 140 °C, respectively (Table S1, Supporting Information). The difference in T_g becomes clearer when we look at the structure of the HTMs. Both organic semiconductors are carbazole derivatives; however, MeO5PECz has an additional bis(4-methoxyphenyl)ethenyl fragment at the 9-position of the carbazole moiety, while MeO4PEBCz has an aliphatic butyl chain

instead, which reduces the bulkiness of the molecule thus lowering the T_g.[41] Furthermore, both materials are partially crystalline with melting temperatures of 204 °C for MeO5PECz and 260 °C for MeO4PEBCz (Figure S2, Supporting Information). Interestingly, during the second heating of MeO5PECz, no crystallization takes place, which is important for the formation of good quality thin films, since spontaneous and uncontrollable crystallization causes charge trapping and layer separation which results in a drop in device efficiency.[42] Although MeO4PEBCz starts to crystallize during the first and second heating, it also possesses relatively high T_g which should lower the probability of the crystallization occurring in a working device quite significantly.

We employed the xerographic time-of-flight (XTOF) method (Figure S4, Supporting Information) to estimate the drift carrier mobility of the investigated pristine materials. The MeO4PEBCz displayed slightly higher mobility of $1.1 \times 10^{-3}\,cm^2\,V^{-1}\,s^{-1}$ versus $7.8 \times 10^{-4}\,cm^2\,V^{-1}\,s^{-1}$ for MeO5PECz under an electric field (Table 1). Despite many similarities between the molecules, the difference in drift carrier mobility could be explained by the closer packing of MeO4PEBCz and consequentially smaller charge hopping distance. This correlates well with the I_p results, since the additional electron donating bis(4-methoxyphenyl) ethenyl moiety in MeO5PECz increases steric hindrance in the molecule and π–π stacking distances, reducing the charge carrier mobility.[43–48]

Four-point probe conductivity measurements were done on MeO5PECz, MeO4PEBCz, and spiro-OMeTAD films with various doping concentrations of Li-TFSI on glass. When undoped, MeO5PECz has around a factor of 10 higher conductivity and MeO4PEBCz has around a factor of 100 higher conductivity compared with pristine spiro-OMeTAD (Figure 1d). For MeO4PEBCz, this is in part due to a mobility that is three times higher, but for both MeO4PEBCz and MeO5PECz, the higher conductivities are mostly attributed to their higher intrinsic doping density compared to pristine spiro-OMeTAD, since conductivity is proportional to both mobility and carrier density. Furthermore, while the conductivity of spiro-OMeTAD increases significantly (approximately three orders of magnitude) with the addition of Li-TFSI, the conductivities of the carbazole-based enamines improve more moderately (approximately two orders of magnitude) up to 250 mol% Li-TFSI. Typically, 50 mol% Li-TFSI is added to spiro-OMeTAD in devices.[49,50] At the highest doping concentrations, MeO4PEBCz is still an order of magnitude more conductive than spiro-OMeTAD.

To probe the quality of the interface between the HTMs and the perovskite absorber layers, we performed absolute photoluminescence (PL) measurements. We determined the external PL quantum efficiency (PLQE) on "half-devices" made with the structure: glass/perovskite/HTM and compared them with films of perovskite on glass (Table S3, Supporting Information, and **Figure 2**). The perovskite absorber material was $FA_{0.83}Cs_{0.17}Pb(I_{0.9}Br_{0.1})_3$ with a bandgap of ≈1.6 eV. Compared with the perovskite films deposited on glass, we observe a reduction in absolute PLQE for all films coated with the charge extraction layers denoting the presence of nonradiative recombination at the transport layer interfaces. Perovskite films coated with the undoped enamine HTMs have the highest PLQE of all the HTM coated samples, while perovskite films coated with the doped enamines show higher PLQE as compared with the doped spiro-OMeTAD. Notably, the perovskite films coated with the undoped MeO5PECz show very little quenching of the PLQE.

From these PLQE measurements, we estimate the quasi-Fermi-level-splitting (QFLS) in the perovskite layer following the method outlined in reference.[51] which is equivalent to the maximum open-circuit voltage (V_{OC}) which could be generated by the perovskite/HTM heterojunction. Specifically, we found the spiro-OMeTAD interface, either doped or undoped, to be the one characterized by the largest amount of recombination losses, limiting the QFLS to ≈1.15 eV for the doped case. Remarkably, when the spiro-OMeTAD is replaced with enamine

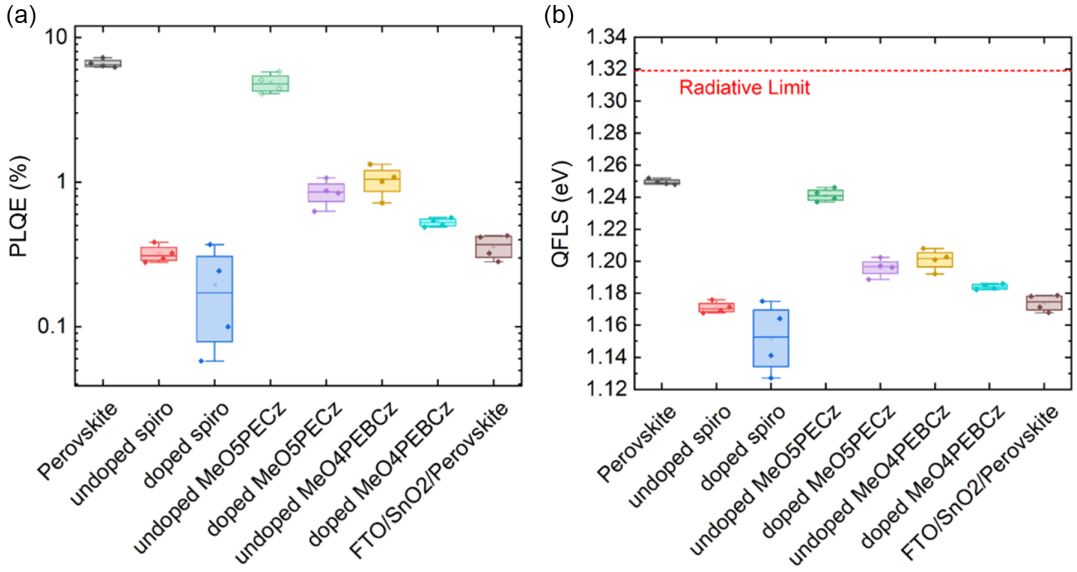

Figure 2. a) PLQE of half stacks on glass with the middle line denoting the median value and the boxes showing 25% –75% range of the data points with the raw data plotted as circles. b) Box plot for the corresponding QFLS calculated using the PLQE.

HTMs, the losses at the HTL interface are significantly reduced, achieving a QFLS as high as 1.24 eV. To examine the perovskite/ETL heterojunction, we also fabricated and measured the PLQE of a sample: FTO/SnO_2/perovskite and calculated the QFLS. In Figure 2, the SnO_2 interface shows significant recombination losses, limiting the QFLS to ≈1.17 eV. These results highlight how both electron transport layer (ETL) and hole transport layer (HTL) interface limit the V_{OC} of *n-i-p* devices, with the conventional materials SnO_2 and spiro-OMeTAD. Since the V_{OC} of a full device stack is limited by its weakest interface, the QFLS results (enamine HTMs > FTO/SnO_2 > spiro-OMeTAD) indicate that spiro-OMeTAD is limiting V_{oc}, but when using enamine HTMs, FTO/SnO_2 becomes the limiting interface.

Across all three of the HTMs, the PLQEs of the perovskite/HTM films consistently drop when Li-TFSI is added to the HTMs (Table S3, Supporting Information, and Figure 2). Contrary to what is often interpreted as more efficient carrier extraction,[51–53] under open-circuit conditions, a higher degree of PL quenching implies increased nonradiative recombination.[19,54] Since our half-devices are not connected to an external circuit, they are operating similarly to a device at open-circuit conditions and the charge carriers only recombine through internal pathways. Since adding Li-TFSI increases the PL quenching, this indicates that adding Li-TFSI increases the rate of nonradiative recombination, which will negatively impact QFLS and as a consequence we would expect this to reduce the Voc in complete devices, if this interface is limiting the *V*oc.

Time-resolved photoluminescence (TRPL) decays were measured via time-correlated single-photon counting (TCSPC) on the same films used for the PLQE measurements, the results of which we show in Figure S10a. Fitting the decays using a stretched-exponential curve (details in the S.I.), we determine a mean carrier lifetime (<τ>) of the PL decay of 308.4 ns for the neat perovskite film coated on glass, 40.2 ns for perovskite films coated with neat spiro-OMeTAD, compared to 160.3 and 52.0 ns for neat MeO5PECz and MeO4PEBCz films, respectively (Table S3, Supporting Information). This varies consistently with the PLQE trends (Figure 2a) and the time-integrated PL spectra (or steady-state PL) (Figure S10b, Supporting Information), indicating for the new enamine-based HTMs, there is less nonradiative recombination introduced at the perovskite/HTM interfaces, in contrast to the perovskite/spiro-OMeTAD heterojunction.

We fabricated *n-i-p* perovskite solar cells with the architecture FTO/SnO_2/$FA_{0.83}Cs_{0.17}Pb(I_{0.9}Br_{0.1})_3$/HTM/Au (**Figure 3**a). Upon investigating doping Li-TFSI and *t*BP into the new carbazole enamine HTMs, we optimized the doping concentrations for each HTM layer. Champion devices made with MeO5PECz achieved a maximum power point tracked efficiency (η_{mpp}) of 17.4% when doped with 33 μL mL^{-1} tBP and 25 mol% Li-TFSI with respect to MeO5PECz (Figure S14a, Supporting Information). Similarly, MeO4PEBCz achieved a η_{mpp} of 16.7% at the same mol% dopant concentrations (Figure S14b, Supporting Information). Due to their high hole mobilities, MeO5PECz and MeO4PEBCz were further tested as dopant-free HTMs. In **Table 2**, we report the devices with the HTMs without dopants, with only *t*BP, and with both *t*BP and Li-TFSI. The *J–V* scans and maximum power point tracked efficiency (η_{mpp}) plots show that the devices made with undoped MeO4PEBCz and MeO5PECz have performances similar to that of devices employing doped spiro-OMeTAD. Without any Li-TFSI or *t*BP doping, MeO4PEBCz achieved a η_{mpp} of 15.9% while MeO5PECz devices achieved a η_{mpp} of 16.1%, as compared with 17.4% with doped spiro-OMeTAD. Notably, there is quite a significant degree of hysteresis among all three devices made with different HTMs. This is partly due to the fast voltage sweep speed (0.61 V s^{-1}) we used in our solar cell measurements. However, the critical figure of merit is the maximum power point tracked efficiency, which reveals the true steady-state efficiency. We also note that significant hysteresis is common in *n-i-p* devices, which has been attributed to a number of factors related to the metal-oxide ETL/perovskite interface.[55–57]

The external quantum efficiency (EQE) spectra are also similar for devices made with the three different HTMs (Figure S12, Supporting Information). Notably, there are some differences in the "wiggles" in the EQE spectra, likely to originate from the difference in the HTM layer thicknesses and coherent interference from the incident and light reflected from the rear Au electrode.

Based on the EQE and PLQE measurements for the full devices made with doped spiro-OMeTAD, undoped MeO5PECz, and MeO4PEBCz, we can perform QFLS analysis on these full devices stacks and compare with the measured V_{oc} to assess the V_{oc} loss in each case (Figure 3b). From the QFLS analysis on the half stacks, we find similar values for the devices fabricated regardless of HTM. As such, this finding highlights that, in a full device, even if the enamine HTMs improve the perovskite/HTL interface, the detrimental SnO_2 interface dominates the V_{OC} losses and the QFLS in a working device. Therefore, as a future study, the ETL/perovskite interface should be concomitantly improved to fully benefit from the HTL optimizations that we report here.

Comparing the QFLS calculated for the full devices to the measured V_{OC} reveals a further loss in the complete devices. In all cases, the measured V_{oc} is lower than the estimated QFLS of the device stack, and this difference is more severe for the cells employing the undoped enamine-based HTMs than those employing the doped spiro-OMeTAD. The difference between the QFLS of the full device stack and the V_{oc} could be explained by either an energetic misalignment between the perovskite and the charge transport layers or the imperfect selectivity of the charge extraction layers.[58,59] From the device results shown in Table 2 and Figure 3b, devices without Li-TFSI and *t*BP dopants in the HTM have higher V_{oc} losses, which contradicts the QFLS results in Figure 2. However, if the ETL/perovskite interface is the dominant recombination channel, the improvements in the HTM will be obscured in the full devices.[59] Furthermore, there could be additional interactions between the dopants added to the HTM and the ETL/perovskite interface, especially under bias where lithium ions can readily diffuse to and alter the ETL/perovskite interface.[29,60] Further studies are required to understand the potential interactions between the dopants and the ETL/perovskite interface.

From the device statistics (Figure S15, Supporting Information), while doping MeO5PECz seems to improve the η_{mpp} of the device, doping MeO4PEBCz does not improve the device efficiency to the same extent. We hypothesize that the higher conductivity of the undoped MeO4PEBCz accounts for the high device performance and removes the need for oxidative

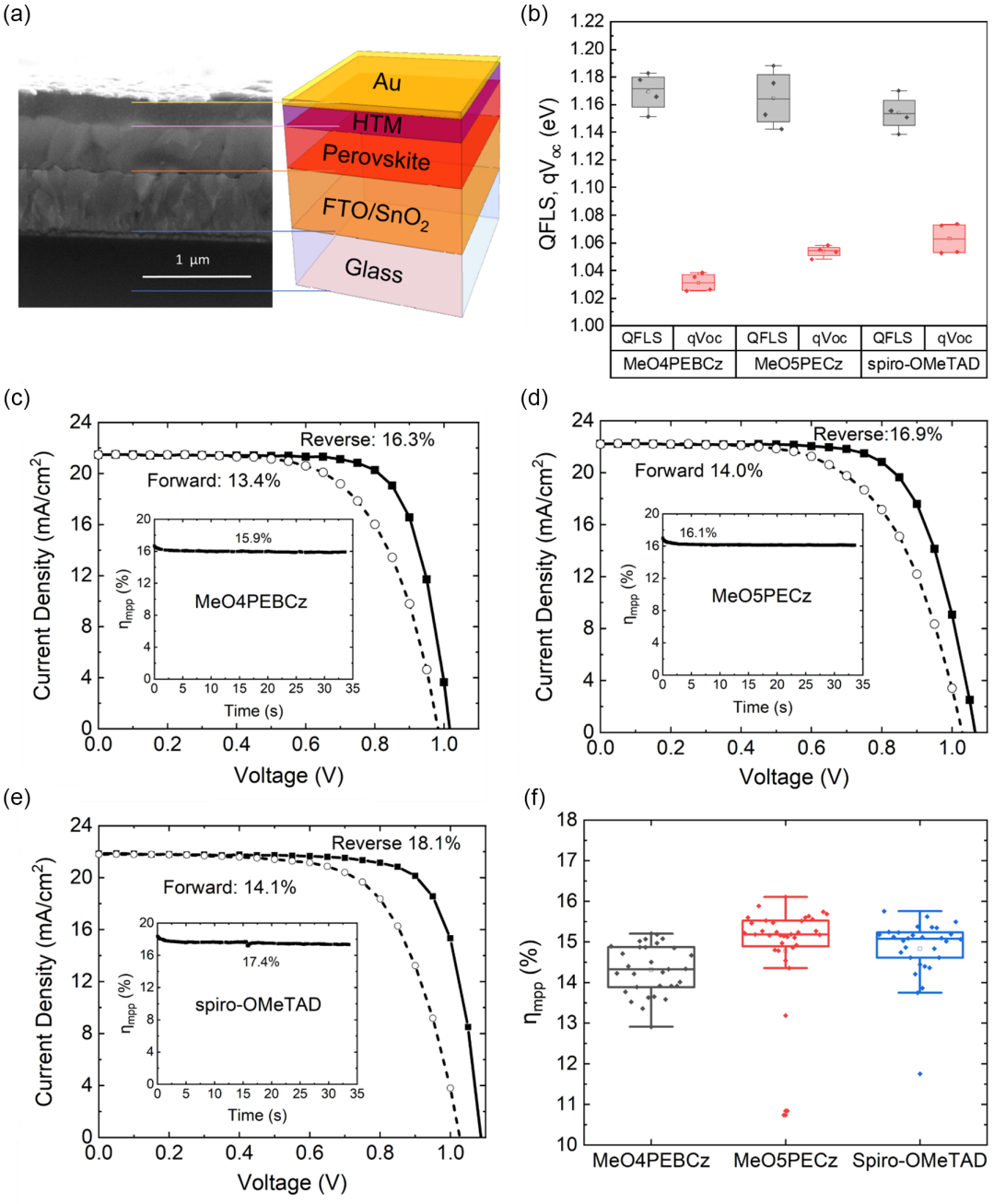

Figure 3. a) Cross-sectional SEM image of a MeO5PECz device and schematic illustration of device stack. b) Calculated quasi-Fermi level splitting (QFLS) of champion full device stacks with the different HTM materials (undoped MeO4PEBCz, undoped MeO5PECz, and doped spiro-OMeTAD, with metallic electrodes) and measured steady-state open-circuit voltage (V_{oc}) of the same perovskite solar cells. We note that the QFLS analysis in Figure 2 was performed on bi-layer films. The *J*–*V* curves of champion devices of c) undoped MeO4PEBCz d) undoped MeO5PECz e) spiro-OMeTAD (doped with Li-TFSI and tBP) as HTMs with their corresponding maximum power point tracked efficiency (η_{mpp}) shown in the insets. f) Statistics of the η_{mpp} for all devices. Spiro-OMeTAD was doped with tBP and Li-TFSI. The MeO5PECz and MeO4PEBCz were undoped.

p-doping. Spiro-OMeTAD and MeO5PECz device efficiencies are improved by approximately 3% (absolute η_{mpp}, Figure S15, Supporting Information) at an optimum concentration of 50 mol% Li-TFSI for spiro-OMeTAD and 25 mol% Li-TFSI for MeO5PECz and 33 µL mL^{-1} *t*BP. In contrast, the performance of MeO4PEBCz devices is not affected by similar doping (25 mol% Li-TFSI and 33 µL mL^{-1} tBP). In fact, higher doping concentration reduces the η_{mpp} of the cells employing MeO4PEBCz. This discrepancy in the effectiveness of doping can be explained by the fact that pristine spiro-OMeTAD has much lower mobility and conductivity than the carbazole-based enamines, and hence requires p-doping to have a suitably low series resistance for the conduction of holes out of the solar cell. In addition to the intrinsic properties of the HTM, another effect

Table 2. Power conversion efficiencies (reverse scans) of champion devices and average performance ± standard deviation (both forward and reverse scans) of a batch of devices fabricated with different HTMs, with or without dopants. The last column shows the maximum power point tracked efficiency (η_{mpp}) for 33 s.

	J_{sc} [mA cm^{-2}]		V_{oc} [V]		FF [%]		PCE [%]		η_{mpp} [%]	
	Best	Average	Best	Average	Best	Average	Best	Average	Best	Average
Undoped MeO4PEBCz	21.9	21.6 ± 0.2	1.02	1.00 ± 0.04	74	65 ± 7	16.4	14.1 ± 1.5	15.9	14.5 ± 0.8
MeO4PEBCz, tBP	21.0	21.0 ± 0.4	1.12	1.04 ± 0.06	72	64 ± 8	16.9	14.5 ± 1.4	17.3	14.8 ± 1.7
MeO4PEBCz, tBP, Li-TFSI	21.3	20.7 ± 0.5	1.09	1.09 ± 0.02	74	68 ± 6	17.0	15.2 ± 1.4	16.7	16.4 ± 0.4
Undoped MeO5PECz	22.2	21.6 ± 0.4	1.06	1.03 ± 0.05	72	63 ± 9	16.9	14.3 ± 1.6	16.1	14.9 ± 1.2
MeO5PECz, tBP	20.9	20.3 ± 0.6	1.09	1.05 ± 0.05	73	67 ± 5	16.5	14.4 ± 1.4	17.0	14.8 ± 1.3
MeO5PECz, tBP, Li-TFSI	20.9	20.4 ± 0.5	1.12	1.10 ± 0.03	74	67 ± 7	17.6	15.0 ± 1.6	17.4	16.2 ± 0.9
Undoped spiro-OMeTAD	21.8	21.7 ± 0.2	1.05	1.01 ± 0.08	66	53 ± 7	15.1	11.6 ± 1.9	14.3	11.7 ± 1.9
Spiro-OMeTAD, tBP, Li-TFSI	21.9	20.5 ± 0.6	1.09	1.01 ± 0.06	76	67 ± 8	18.1	14.6 ± 2.1	17.4	15.5 ± 0.9

that could explain why the PCEs of devices employing spiro-OMeTAD increase significantly upon doping, is that the optimized spiro-OMeTAD layer (200 nm) is thicker than the undoped carbazole-based enamine layers (45∼55 nm). Predictably, doping is more necessary for thicker transport layers because the resistance through the layer will increase linearly with increasing thickness, causing a fill factor drop in devices.[19] The series resistance could be reduced by decreasing the spiro-OMeTAD layer thickness, but at a cost of introducing pinholes and lowering shunt resistance; since, this material is not effective at forming continuous films when the thickness is decreased. Hence, the ability to form a continuous film in a thin layer is another important property of these carbazole-based enamines HTMs.

Since these new HTMs perform well without dopants and have higher glass-transition temperatures (T_g) than spiro-OMeTAD, we carried out stability studies on complete solar cells. The *n-i-p* device stack (shown in Figure 3a) was modified for better stability by introducing a phenyl-C61-butyric acid methyl ester (PCBM) interlayer between the SnO_2 and the perovskite absorber layer: glass/FTO/SnO_2/PCBM/$FA_{0.83}Cs_{0.17}Pb(I_{0.9}Br_{0.1})$/HTM/Au. Upon the addition of a PCBM layer, there is no significant difference in the device performance aside from a slight enhancement in the V_{oc} (Figure S16, Supporting Information). Devices with three different HTMs: spiro-OMeTAD doped with Li-TFSI and *t*BP, undoped MeO5PECz, and undoped MeO4PEBCz were aged at 85 °C in a nitrogen atmosphere (**Figure 4**a). While devices employing spiro-OMeTAD showed fast degradation within the first 24 h, the devices employing the two new carbazole-based enamines exhibited a striking contrast—they improved in efficiency over the first 100 h and maintained >80% of their peak performance after 1,000 h. Thermal degradation of spiro-OMeTAD devices has been reported in the literature and has been shown to be caused by the formation of voids at the spiro-OMeTAD/ perovskite interface,[32,33,61] post iodine doping of spiro-OMeTAD from the perovskite film during aging,[62] *t*BP reacting with spiro-OMeTAD forming new pyridinated species,[63,64] and spiro-OMeTAD recrystallizing at 85 °C due to its low glass transition temperature.[42,65,66]

There have been many tests and exemplifications of good stability of perovskite solar cells, in both the *p-i-n* and *n-i-p* configuration, stressed under simulated sunlight at normal operating temperatures.[67,68] However, the combination of temperature and light is particularly stressful for perovskite solar cells. Although there have been very encouraging results for ambient 65 and 85 °C full-spectrum light soaking for *p-i-n* cells,[69,70] there have been few reports of stress tests of *n-i-p* cells under combined (heat and light) stress conditions. There are some reports of *n-i-p* device stability with SnO_2 under combined light and 65 °C in a nitrogen atmosphere[71] or 55 °C ambient light stability test.[72] Herein, we assess the stability of our *n-i-p* perovskite solar cells comprising the three different HTMs, encapsulated and subject to full-spectrum 1 sun irradiance at 85 °C (±3 °C) in ambient conditions; the results of which we show in Figure 4b. Unfortunately, all the devices degraded rapidly under the combination of thermal and light stress, however, the degradation trends are somewhat different. The devices made with the new carbazole-based HTMs improved in the initial 24 h of aging and then gradually degraded; whereas, spiro-OMeTAD-based devices degraded rapidly from the beginning. These results are consistent with the thermally driven degradation due to the spiro-OMeTAD HTM dominating the first 24 h of aging, but a further degradation mechanism takes over when devices are stressed for longer times under light at elevated temperatures. We postulate that reactions and degradations at the perovskite/n-type layer heterojunction are driving this degradation under light and temperature.

To probe the influence of atmosphere (humidity and oxygen) upon the illuminated cells, we subject complete unencapsulated devices to LED white light illumination with close to 0.6 sun equivalent irradiance, in air at 40 °C, under open-circuit conditions. In Figure 4c, we show photographs taken at the end of 7 days of aging under the LED light. After stressing, the gold contacts on top of the spiro-OMeTAD devices have become visible from the glass side; whereas, the devices employing MeO5PECz and MeO4PEBCz remain opaque, since the perovskite beneath the new HTMs remains black. This indicates that some form of electrochemical or galvanostatic degradation is taking place within the devices employing

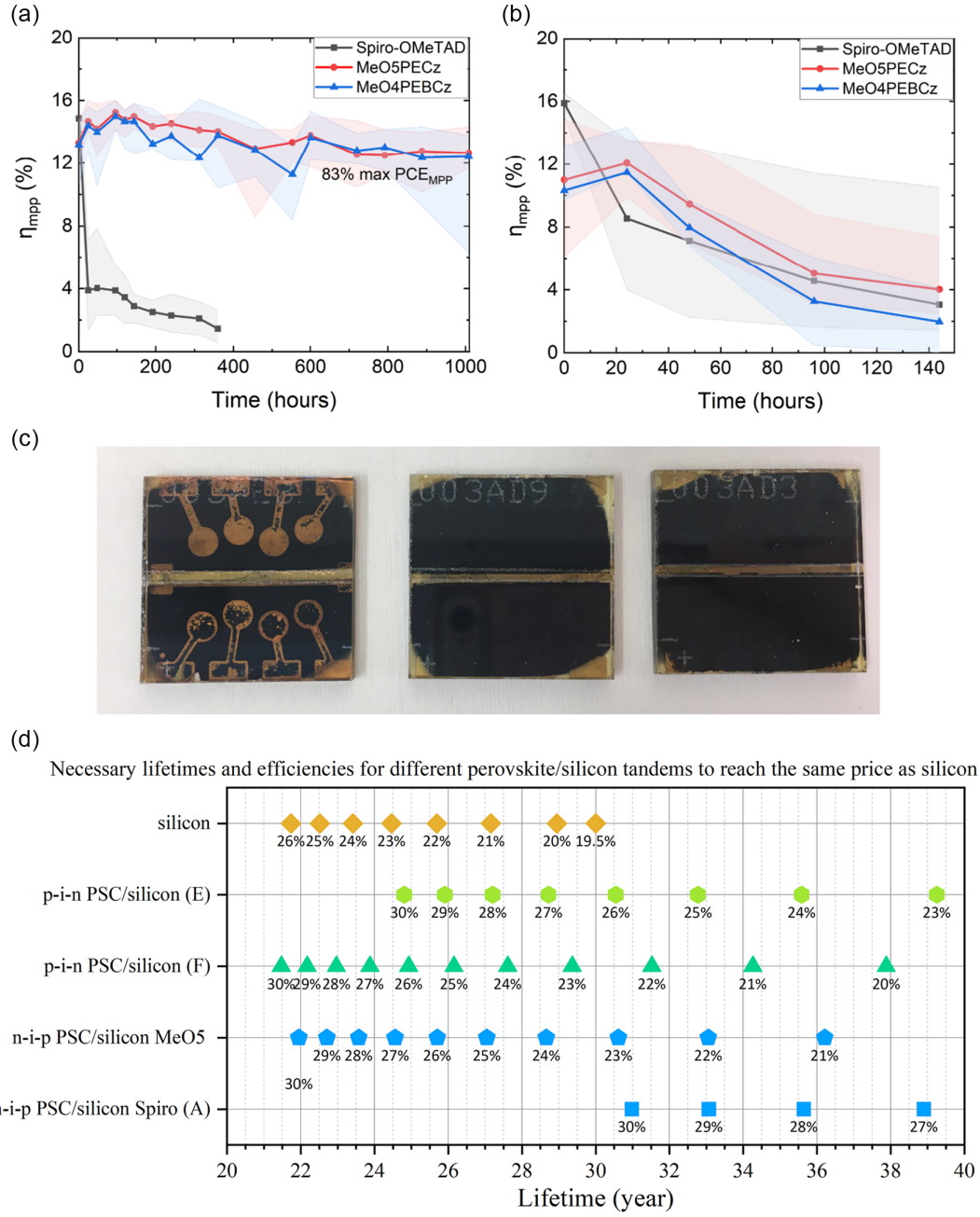

Figure 4. a) 85 °C dark aging under a nitrogen atmosphere, removed occasionally and tested at room temperature in air, with max power point tracked efficiency shown, averaged over 18 devices. b) Average efficiency as a function of time for encapsulated perovskite cells aged under AM1.5 full spectrum sunlight (xenon lamp Suntest aging box) at 76 mW cm^{-2} irradiance at 85 °C. c) Photograph of (unencapsulated) devices after 7 days of ambient LED light aging (with 60 mW cm^{-2} intensity under 40 °C). d) Cost calculation for different perovskite tandem solar cells to reach the same cost as a silicon module. Architecture **A** is a homojunction-based tandem with the perovskite solar cell being SnO_2/perovskite/Spiro-OMeTAD/MoO_x/ITO/Ag. The architecture with MeO5PECz is the same as A, the only difference is that spiro-OMeTAD is replaced with MeO5PECz. **E** is a heterojunction-based tandem with the perovskite solar cell being NiO_x/polyTPD/PFN/perovskite/LiF/C60/SnO_x/ITO/Ag and **F** is the same but a simpler perovskite solar cell with NiO_x/perovskite/C60/SnO_x/ITO/Ag. Each given point shows the necessary lifetime and module efficiency which one would need to reach the same cost (0.11 \$ kWh^{-1}) as a 19.5% efficient silicon solar module (the capacity-weighted average monocrystalline module efficiency in Q1 2020 according to CA NEM reports[74]) in Phoenix, Arizona which lasts for 30 years.

Li-TFSI and *t*BP doped spiro-OMeTAD, possibly driven by the migration of water and/or lithium ions into the active layer of the device.[73]

These results illustrate that although we have now achieved thermally stable *n-i-p* cells with the new HTMs and improved stability under light soaking in ambient conditions, the issue of good stability under combined light and elevated temperature remains unsolved. We hypothesize that further improvements to the n-type ETL/perovskite heterojunction and the electrodes are now required, in order to deliver competitively stable *n-i-p* perovskite solar cells.

Finally, we want to understand the scale of the impact of the lower cost of the HTMs on the final PV module production and electricity generation costs. Recently, Chang et al.[39] found that spiro-OMeTAD would be the highest single contributor to cost, by a significant margin, if employed in perovskite solar cells and perovskite/silicon tandems. As outlined previously, it is possible to lower the manufacturing cost of the HTM by around one order of magnitude from 92 \$ g^{-1} for spiro-OMeTAD to 10.33 \$ g^{-1} for MeO4PEBCz and 7.83 \$ g^{-1} for MeO5PECz (Table S4 and S5, Supporting Information). To study what that means for the final commercialized module, we perform a cost analysis. We note that this methodology gives the means to compare different PV technologies. However, since there are many assumptions in the calculations which can only be estimated at this stage, such as material processing and cost reductions with increasing scale, the results of our estimations cannot be taken as absolute values. We first took the (capacity weighted average) manufacturing costs of silicon PV, in $\$/W_{DC,}$ from the 2020 NREL PV benchmark report and calculated the levelized cost of electricity (LCOE) for a silicon PV module deployed in a residential installation in Phoenix, Arizona, in order[74] to verify that the parameters of our cost model are sensible. We determined an LCOE of 0.11 \$ kWh^{-1}, the same as the NREL PV benchmark report, confirming that our methodology is consistent with others. Among other factors, the LCOE depends on the manufacturing cost, which is the only PV technology-specific aspect which we will vary in our model here. Thus, it's possible to express the manufacturing cost as a function of the lifetime (T_{80} time) and efficiency required to achieve a given LCOE. We set the LCOE at 0.11 \$ kWh^{-1} and show a plot of the manufacturing costs against the required lifetime to achieve such LCOE, for a range of different efficiencies of PV modules in Figure S19, Supporting Information. We also show the calculated manufacturing costs for a range of different perovskite-on-silicon tandem modules (architectures A, F, and G), as estimated by Chang et al.,[39] the costs of a single junction silicon module and our estimated cost for the tandem modules incorporating MeO5PECz, our best performing HTM. In order to achieve this LCOE, the single junction Si module lasts for 30 years at a starting efficiency of 19.5% (the USA capacity-weighted average efficiency for Si PV modules).[74] It is apparent that the lifetime required to obtain an LCOE of 0.11 \$ kWh^{-1} for a perovskite PV module employing spiro-OMeTAD, is considerably longer than 40 years, even at the highest efficiency model of 30%. However, for our device structure employing MeO5PECz, this LCOE can be achieved within a feasible range of lifetimes and an attainable range of efficiencies, such as 25 years lifetime at 27% starting efficiency. We summarize the results in Figure 4d, where we show the efficiencies required to reach the LCOE target, for different lifetimes and for different module architectures.

3. Conclusions

We have presented the synthesis of two new carbazole-based enamines HTMs. These HTMs can be obtained in a simple synthesis procedure from commercially available materials and without the use of expensive palladium-catalyzed cross-coupling reactions. Moreover, none of the investigated compounds required column chromatography or any other expensive purification techniques, making them more than tenfold cheaper at research volumes than spiro-OMeTAD. Both new carbazole-based enamine materials are thermally stable, have high T_g, suitable energy levels and bandgap, and relatively high charge carrier mobilities (up to 1.1×10^{-3} $cm^2 V^{-1} s^{-1}$), negating the need for dopant additives in the solar cells.

We demonstrated devices made with MeO5PECz and MeO4PEBCz that can reach >16% PCEs without adding Li-TFSI or *t*BP into the HTM solutions. Through QFLS analysis, we have revealed that significant further improvements in both Voc and efficiency will be possible by focusing future efforts upon improving the ETL/Perovskite interface in conjunction with employing the new HTMs reported here. Leaving out Li-TFSI and *t*BP additives improves the device's moisture and thermal stability, since no hygroscopic additives are present, and no volatile dopants can escape under elevated temperature nor react with the perovskite. The low synthetic cost and less material required in the optimized devices make the new HTMs significantly more economically viable to integrate into perovskite solar cell devices and tandem modules. Furthermore, the simplicity of synthesis and high operational stability of devices may make these HTMs the new standard HTMs for perovskite PV research going forward.

Supporting Information

Supporting Information is available from the Wiley Online Library or from the author.

Acknowledgements

The research leading to these results had received funding from the European Union's Horizon 2020 research and innovation program under grant agreement no. 763977 of the PerTPV project and the Marie Skłodowska-Curie grant agreement no. 764787 of the MAESTRO project. V.G., M.S., and T.M. acknowledge funding from the Research Council of Lithuania under grant agreement Nr. 01.2.2-LMT-K-718-03-0040 (SMARTMOLECULES) and thank Dr. E. Kamarauskas for ionization potential measurements. The research from this author has received funding from the rank prize funding. This work also received funding from the EPSRC UK under project EP/S004947/1. The authors thank Nathan Chang for his helpful input and Nobuya Sakai and Manuel Kober-Czerny for suggestions on analyzing photoluminescence data.

Conflict of Interest

The authors declare no conflict of interest.

Data Availability Statement

The data that support the findings of this study are available from the corresponding authors upon reasonable request.

Keywords

chemical oxidation, enamines, hole transporting materials, low-cost synthesis, perovskite solar cells, perovskites

Received: November 29, 2021
Published online: December 11, 2021

[1] A. Kojima, K. Teshima, Y. Shirai, T. Miyasaka, *J. Am. Chem. Soc.* **2009**, *131*, 6050.
[2] H. S. Kim, C. R. Lee, J. H. Im, K. B. Lee, T. Moehl, A. Marchioro, S. J. Moon, R. Humphry-Baker, J. H. Yum, J. E. Moser, M. Grätzel, N. G. Park, *Sci. Rep.* **2012**, *2*, 591.
[3] M. M. Lee, J. Teuscher, T. Miyasaka, T. N. Murakami, H. J. Snaith, *Science* **2012**, *338*, 643.
[4] M. A. Green, E. D. Dunlop, J. Hohl-Ebinger, M. Yoshita, N. Kopidakis, A. W. Y. Ho-Baillie, *Prog. Photovoltaics Res. Appl.* **2020**, *28*, 3.
[5] J. J. Yoo, G. Seo, M. R. Chua, T. G. Park, Y. Lu, F. Rotermund, Y.-K. Kim, C. S. Moon, N. J. Jeon, J.-P. Correa-Baena, V. Bulović, S. S. Shin, M. G. Bawendi, J. Seo, *Nature* **2021**, *590*, 587.
[6] H. Min, M. Kim, S.-U. Lee, H. Kim, G. Kim, K. Choi, J. H. Lee, S. Il Seok, *Science* **2019**, *366*, 749.
[7] G. Kim, H. Min, K. S. Lee, D. Y. Lee, S. M. Yoon, S. Il Seok, *Science* **2020**, *370*, 108.
[8] U. Bach, D. Lupo, P. Comte, J. E. Moser, F. Weissörtel, J. Salbeck, H. Spreitzer, M. Grätzel, *Nature* **1998**, *395*, 583.
[9] T. Leijtens, G. E. Eperon, N. K. Noel, S. N. Habisreutinger, A. Petrozza, H. J. Snaith, *Adv. Energy Mater.* **2015**, *5*, 1500963.
[10] W. Nie, J.-C. Blancon, A. J. Neukirch, K. Appavoo, H. Tsai, M. Chhowalla, M. A. Alam, M. Y. Sfeir, C. Katan, J. Even, S. Tretiak, J. J. Crochet, G. Gupta, A. D. Mohite, *Nat. Commun.* **2016**, *7*, 1.
[11] G. Divitini, S. Cacovich, F. Matteocci, L. Cinà, A. Di Carlo, C. Ducati, *Nat. Energy* **2016**, *1*, 1.
[12] M. Salado, L. Contreras-Bernal, L. Caliò, A. Todinova, C. López-Santos, S. Ahmad, A. Borras, J. Idígoras, J. A. Anta, *J. Mater. Chem. A* **2017**, *5*, 10917.
[13] A. Solanki, P. Yadav, S. H. Turren-Cruz, S. S. Lim, M. Saliba, T. C. Sum, *Nano Energy* **2019**, *58*, 604.
[14] G. E. Eperon, S. N. Habisreutinger, T. Leijtens, B. J. Bruijnaers, J. J. Van Franeker, D. W. Dequilettes, S. Pathak, R. J. Sutton, G. Grancini, D. S. Ginger, R. A. J. Janssen, A. Petrozza, H. J. Snaith, *ACS Nano* **2015**, *9*, 9380.
[15] D. Wang, M. Wright, N. K. Elumalai, A. Uddin, *Sol. Energy Mater. Sol. Cells* **2016**, *147*, 255.
[16] A. M. A. Leguy, Y. Hu, M. Campoy-Quiles, M. I. Alonso, O. J. Weber, P. Azarhoosh, M. van Schilfgaarde, M. T. Weller, T. Bein, J. Nelson, P. Docampo, P. R. F. Barnes, *Chem. Mater.* **2015**, *27*, 3397.
[17] H. Kim, K.-G. Lim, T.-W. Lee, *Energy Environ. Sci.* **2016**, *9*, 12.
[18] W. Zhang, F. Zhang, B. Xu, Y. Li, L. Wang, B. Zhang, Y. Guo, J. M. Gardner, L. Sun, L. Kloo, *ACS Appl. Mater. Interfaces* **2020**, *12*, 33751.
[19] T. Du, W. Xu, M. Daboczi, J. Kim, S. Xu, C. T. Lin, H. Kang, K. Lee, M. J. Heeney, J. S. Kim, J. R. Durrant, M. A. McLachlan, *J. Mater. Chem. A* **2019**, *7*, 18971.
[20] J. Burschka, A. Dualeh, F. Kessler, E. Baranoff, N. L. Cevey-Ha, C. Yi, M. K. Nazeeruddin, M. Grätzel, *J. Am. Chem. Soc.* **2011**, *133*, 18042.
[21] M. D. Irwin, D. B. Buchholz, A. W. Hains, R. P. H. Chang, T. J. Marks, *Proc. Natl. Acad. Sci. U.S.A.* **2008**, *105*, 2783.
[22] J. H. Noh, N. J. Jeon, Y. C. Choi, M. K. Nazeeruddin, M. Grätzel, S. Il Seok, *J. Mater. Chem. A* **2013**, *1*, 11842.
[23] A. Abate, T. Leijtens, S. Pathak, J. Teuscher, R. Avolio, M. E. Errico, J. Kirkpatrik, J. M. Ball, P. Docampo, I. McPherson, H. J. Snaith, *Phys. Chem. Chem. Phys.* **2013**, *15*, 2572.
[24] J.-Y. Seo, H.-S. Kim, S. Akin, M. Stojanovic, E. Simon, M. Fleischer, A. Hagfeldt, S. M. Zakeeruddin, M. Grätzel, *Energy Environ. Sci.* **2018**, *11*, 2985.
[25] N. Sakai, R. Warren, F. Zhang, S. Nayak, J. Liu, S. V. Kesava, Y.-H. Lin, H. S. Biswal, X. Lin, C. Grovenor, T. Malinauskas, A. Basu, T. D. Anthopoulos, V. Getautis, A. Kahn, M. Riede, P. K. Nayak, H. J. Snaith, *Nat. Mater.* **2021**, *20*, 1248.
[26] T. H. Schloemer, J. A. Christians, J. M. Luther, A. Sellinger, *Chem. Sci.* **2019**, *10*, 1904.
[27] Z. Song, J. Liu, G. Wang, W. Zuo, C. Liao, J. Mei, *ChemPhysChem* **2017**, *18*, 3030.
[28] Y. Cho, H. Do Kim, J. Zheng, J. Bing, Y. Li, M. Zhang, M. A. Green, A. Wakamiya, S. Huang, H. Ohkita, A. W. Y. Ho-Baillie, *ACS Energy Lett.* **2021**, *6*, 925.
[29] Z. Li, C. Xiao, Y. Yang, S. P. Harvey, D. H. Kim, J. A. Christians, M. Yang, P. Schulz, S. U. Nanayakkara, C.-S. Jiang, J. M. Luther, J. J. Berry, M. C. Beard, M. M. Al-Jassim, K. Zhu, *Energy Environ. Sci.* **2017**, *10*, 1234.
[30] S. Wang, W. Yuan, Y. S. Meng, *ACS Appl. Mater. Interfaces* **2015**, *7*, 24791.
[31] H.-S. Kim, J.-Y. Seo, N.-G. Park, *ChemSusChem* **2016**, *9*, 2528.
[32] A. K. Jena, Y. Numata, M. Ikegami, T. Miyasaka, *J. Mater. Chem. A* **2018**, *6*, 2219.
[33] A. K. Jena, M. Ikegami, T. Miyasaka, *ACS Energy Lett.* **2017**, *2*, 1760.
[34] Y. Ko, Y. Kim, C. Lee, Y. Kim, Y. Jun, *ACS Appl. Mater. Interfaces* **2018**, *10*, 11633.
[35] K. Rakstys, C. Igci, M. K. Nazeeruddin, *Chem. Sci.* **2019**, *10*, 6748.
[36] D. Bharath, M. Sasikumar, N. R. Chereddy, J. R. Vaidya, S. Pola, *Sol. Energy* **2018**, *174*, 130.
[37] A. Al-Ashouri, A. Magomedov, M. Roß, M. Jošt, M. Talaikis, G. Chistiakova, T. Bertram, J. A. Márquez, E. Köhnen, E. Kasparavičius, S. Levcenco, L. Gil-Escrig, C. J. Hages, R. Schlatmann, B. Rech, T. Malinauskas, T. Unold, C. A. Kaufmann, L. Korte, G. Niaura, V. Getautis, S. Albrecht, *Energy Environ. Sci.* **2019**, *12*, 3356.
[38] R. Azmi, S. Y. Nam, S. Sinaga, Z. A. Akbar, C.-L. Lee, S. C. Yoon, I. H. Jung, S.-Y. Jang, *Nano Energy* **2018**, *44*, 191.
[39] N. L. Chang, J. Zheng, Y. Wu, H. Shen, F. Qi, K. Catchpole, A. Ho-Baillie, R. J. Egan, *Prog. Photovoltaics Res. Appl.* **2021**, *29*, 401.
[40] M. C. Alonso García, J. L. Balenzategui, *Renew. Energy* **2004**, *29*, 1997.
[41] R. Lygaitis, V. Getautis, J. V. Grazulevicius, *Chem. Soc. Rev.* **2008**, *37*, 770.
[42] X. Zhao, H.-S. Kim, J.-Y. Seo, N.-G. Park, *ACS Appl. Mater. Interfaces* **2017**, *9*, 7148.
[43] K. Kawabata, M. Saito, N. Takemura, I. Osaka, K. Takimiya, *Polym. J.* **2017**, *49*, 169.
[44] B. Fu, J. Baltazar, A. R. Sankar, P.-H. Chu, S. Zhang, D. M. Collard, E. Reichmanis, *Adv. Funct. Mater.* **2014**, *24*, 3734.
[45] A.-R. Han, G. K. Dutta, J. Lee, H. R. Lee, S. M. Lee, H. Ahn, T. J. Shin, J. H. Oh, C. Yang, *Adv. Funct. Mater.* **2015**, *25*, 247.
[46] J. Mei, H.-C. Wu, Y. Diao, A. Appleton, H. Wang, Y. Zhou, W.-Y. Lee, T. Kurosawa, W.-C. Chen, Z. Bao, *Adv. Funct. Mater.* **2015**, *25*, 3455.
[47] I. Kang, H. J. Yun, D. S. Chung, S. K. Kwon, Y. H. Kim, *J. Am. Chem. Soc.* **2013**, *135*, 14896.
[48] J. Mei, D. H. Kim, A. L. Ayzner, M. F. Toney, Z. Bao, *J. Am. Chem. Soc.* **2011**, *133*, 20130.

[49] M. Saliba, J.-P. Correa-Baena, C. M. Wolff, M. Stolterfoht, N. Phung, S. Albrecht, D. Neher, A. Abate, *Chem. Mater.* **2018**, *30*, 4193.
[50] D. Payno, M. Salado, M. Andresini, D. Gutiérrez-Moreno, P. Huang, F. Ciriaco, S. Kazim, Á. Sastre-Santos, F. Fernández-Lázaro, S. Ahmad, *Emergent Mater.* **2021**, *1*, 1.
[51] M. Salado, J. Idigoras, L. Calio, S. Kazim, M. K. Nazeeruddin, J. A. Anta, S. Ahmad, *ACS Appl. Mater. Interfaces* **2016**, *8*, 34414.
[52] J. Cao, S. Mo, X. Jing, J. Yin, J. Li, N. Zheng, *Nanoscale* **2016**, *8*, 3274.
[53] S. Sidhik, D. Esparza, A. Martínez-Benítez, T. Lopez-Luke, R. Carriles, I. Mora-Sero, E. De La Rosa, *J. Phys. Chem. C* **2017**, *121*, 4239.
[54] V. M. Le Corre, M. Stolterfoht, L. Perdigón Toro, M. Feuerstein, C. Wolff, L. Gil-Escrig, H. J. Bolink, D. Neher, L. J. A. Koster, *ACS Appl. Energy Mater.* **2019**, *2*, 6280.
[55] P. Song, L. Shen, L. Zheng, K. Liu, W. Tian, J. Chen, Y. Luo, C. Tian, L. Xie, Z. Wei, *Nano Sel.* **2021**, *2*, 1779.
[56] D. Yang, R. Yang, K. Wang, C. Wu, X. Zhu, J. Feng, X. Ren, G. Fang, S. Priya, S. (Frank) Liu, *Nat. Commun.* **2018**, *919*, 1.
[57] T. Bu, J. Li, F. Zheng, W. Chen, X. Wen, Z. Ku, Y. Peng, J. Zhong, Y. B. Cheng, F. Huang, *Nat. Commun.* **2018**, *9*, 1.
[58] P. Caprioglio, M. Stolterfoht, C. M. Wolff, T. Unold, B. Rech, S. Albrecht, D. Neher, *Adv. Energy Mater.* **2019**, *9*, 1901631.
[59] M. Stolterfoht, P. Caprioglio, C. M. Wolff, J. A. Márquez, J. Nordmann, S. Zhang, D. Rothhardt, U. Hörmann, Y. Amir, A. Redinger, L. Kegelmann, F. Zu, S. Albrecht, N. Koch, T. Kirchartz, M. Saliba, T. Unold, D. Neher, *Energy Environ. Sci.* **2019**, *12*, 2778.
[60] M. Kim, I. Choi, S. J. Choi, J. W. Song, S.-I. Mo, J.-H. An, Y. Jo, S. Ahn, S. K. Ahn, G.-H. Kim, D. S. Kim, *Joule* **2021**, *5*, 659.
[61] S. Wang, M. Sina, P. Parikh, T. Uekert, B. Shahbazian, A. Devaraj, Y. S. Meng, *Nano Lett.* **2016**, *16*, 5594.
[62] G. Tumen-Ulzii, C. Qin, T. Matsushima, M. R. Leyden, U. Balijipalli, D. Klotz, C. Adachi, *Sol. RRL* **2020**, *4*, 2000305.
[63] A. Magomedov, E. Kasparavičius, K. Rakstys, S. Paek, N. Gasilova, K. Genevičius, G. Juška, T. Malinauskas, M. K. Nazeeruddin, V. Getautis, *J. Mater. Chem. C* **2018**, *6*, 8874.
[64] F. Lamberti, T. Gatti, E. Cescon, R. Sorrentino, A. Rizzo, E. Menna, G. Meneghesso, M. Meneghetti, A. Petrozza, L. Franco, *Chem* **2019**, *5*, 1806.
[65] E. Kasparavicius, A. Magomedov, T. Malinauskas, V. Getautis, *Chem. - Eur. J.* **2018**, *24*, 9910.
[66] T. Malinauskas, D. Tomkute-Luksiene, R. Sens, M. Daskeviciene, R. Send, H. Wonneberger, V. Jankauskas, I. Bruder, V. Getautis, *ACS Appl. Mater. Interfaces* **2015**, *7*, 11107.
[67] J. A. Christians, P. Schulz, J. S. Tinkham, T. H. Schloemer, S. P. Harvey, B. J. T. de Villers, A. Sellinger, J. J. Berry, J. M. Luther, *Nat. Energy* **2018**, *3*, 68.
[68] J. Yin, J. Cao, X. He, S. Yuan, S. Sun, J. Li, N. Zheng, L. Lin, *J. Mater. Chem. A* **2015**, *3*, 16860.
[69] S. Bai, P. Da, C. Li, Z. Wang, Z. Yuan, F. Fu, M. Kawecki, X. Liu, N. Sakai, J. T.-W. Wang, S. Huettner, S. Buecheler, M. Fahlman, F. Gao, H. J. Snaith, *Nature* **2019**, *571*, 245.
[70] Y. H. Lin, N. Sakai, P. Da, J. Wu, H. C. Sansom, A. J. Ramadan, S. Mahesh, J. Liu, R. D. J. Oliver, J. Lim, L. Aspitarte, K. Sharma, P. K. Madhu, A. B. Morales-Vilches, P. K. Nayak, S. Bai, F. Gao, C. R. M. Grovenor, M. B. Johnston, J. G. Labram, J. R. Durrant, J. M. Ball, B. Wenger, B. Stannowski, H. J. Snaith, *Science* **2020**, *369*, 96.
[71] M. M. Tavakoli, M. Saliba, P. Yadav, P. Holzhey, A. Hagfeldt, S. M. Zakeeruddin, M. Grätzel, *Adv. Energy Mater.* **2019**, *9*, 1802646.
[72] E. Akman, S. Akin, *Adv. Mater.* **2021**, *33*, 2006087.
[73] E. M. Sanehira, B. J. T. de Villers, P. Schulz, M. O. Reese, S. Ferrere, K. Zhu, L. Y. Lin, J. J. Berry, J. M. Luther, *ACS Energy Lett.* **2016**, *1*, 38.
[74] D. Feldman, V. Ramasamy, R. Fu, A. Ramdas, J. Desai, R. Margolis, *U.S. Solar Photovoltaic System and Energy Storage Cost Benchmark: Q1 2020*, National Renewable Energy Laboratory, Golden, CO **2021**.